The Astrophysical Journal, 902:31 (10pp), 2020 October 10 https://doi.org/10.3847/1538-4357/abb36e

On the Coronal Temperature in Solar Microflares

Paola Testa[1] and Fabio Reale[2,3]
[1] Harvard–Smithsonian Center for Astrophysics, 60 Garden St., Cambridge, MA 02193, USA; ptesta@cfa.harvard.edu
[2] Dipartimento di Fisica e Chimica, Università di Palermo, Piazza del Parlamento 1, I-90134 Palermo, Italy; fabio.reale@unipa.it
[3] INAF-Osservatorio Astronomico di Palermo, Piazza del Parlamento 1, I-90134 Palermo, Italy
Received 2020 June 26; revised 2020 August 7; accepted 2020 August 26; published 2020 October 8

Abstract

We present a study of solar imaging and spectral observations of a microflare, focusing on the temperature diagnostics provided by the Atmospheric Imaging Assembly (AIA) on board the Solar Dynamics Observatory, and the Extreme-Ultraviolet Imaging Spectrometer (EIS) on board Hinode. Our data analysis, in particular from the emission in the 131 and 94 Å channels, indicates that the heated plasma reaches temperatures of $\gtrsim$10 MK, at odds with a previous analysis of the same event, and we discuss the reason for the discrepancy. A particularly interesting aspect is the likely presence of the Fe XXIII 263.76 Å line, though weak, in EIS spectra in the early phases of the event, supporting the presence of high temperature plasma. Hydrodynamic 1D modeling of a single loop heated with a 3 minute pulse to 12–15 MK reproduces well most observed features along one of the brightening loops, including intensities in the AIA hot channels and their temporal variability, as well as the intensity, Doppler shift, and line width of the EIS Fe XXIII line, and its timing relative to the AIA emission. Overall, we obtain a coherent scenario of a typical microflaring loop system and provide constraints on the intensity of the energy release as well as its spatial and temporal distribution, both along and across the loop.

Unified Astronomy Thesaurus concepts: Active solar corona (1988); Solar corona (1483); Solar active regions (1974); Solar coronal heating (1989); Solar coronal loops (1485); Solar extreme ultraviolet emission (1493)

1. Introduction

The details of the processes heating the solar corona to millions of degrees are still poorly understood (e.g., Klimchuk 2006; Testa et al. 2015), and are expected to reveal which physical mechanisms might be dominating in different solar coronal features, e.g., in quiet Sun versus active regions.

The hottest coronal plasma observed typically resides in the core of active regions. The hot AR core plasma is generally observed to be very transient (e.g., Testa & Reale 2012; Testa et al. 2013; Ugarte-Urra & Warren 2014; Graham et al. 2019; Ugarte-Urra et al. 2019), also outside large flares. The Atmospheric Imaging Assembly (AIA; Lemen et al. 2012) on board the Solar Dynamics Observatory (SDO; Pesnell et al. 2012) has significantly contributed to the study of hot coronal plasma in active region cores, especially with the 94 Å channel, which contains a hot Fe XVIII line (at ∼93.93 Å) with peak formation temperature around Log $T[K] \sim 6.9$. However, given the possible contribution of other lines (e.g., Foster & Testa 2011; Boerner et al. 2012; Testa et al. 2012) and the broad contribution function of this line, the determination of the typical temperature of formation of the 94 Å emission observed in AIA has been the focus of many studies (e.g., Testa & Reale 2012; Teriaca et al. 2012). Several approaches have been used to isolate the Fe XVIII emission in the AIA 94 Å images (e.g., Reale et al. 2011; Testa & Reale 2012; Warren et al. 2012; Del Zanna 2013).

An accurate determination of the high temperature component in AR emission has crucial relevance in constraining coronal heating (e.g., Klimchuk 2006; Reale 2014; Barnes et al. 2016).

The topic of the temperature reached by small heating events leading to hot AR core loops observed in AIA 94 Å is still very much debated (e.g., Mitra-Kraev & Del Zanna 2019; Reale et al. 2019a; Testa et al. 2020). We recently studied a sample of nano/microflare events, identified by the presence of hot loops (bright in AIA 94 and 131 Å) for which we derived typical peak temperatures of the order of 8–10 MK, even for the smallest events (Reale et al. 2019a, 2019b; Testa et al. 2020). This is in contrast with a recently published analysis of a microflare observed with AIA and Hinode/EIS (Mitra-Kraev & Del Zanna 2019), which derives rather low (4.5–5 MK) peak coronal temperatures for that event. There is growing observational evidence that at least the hottest plasma component in active region cores is heated by impulsive energy releases likely caused by magnetic reconnection. These impulsive heating events are likely characterized by a wide range of properties (e.g., total energy release and duration of energy release), which can in principle lead in turn to a broad range of plasma temperatures reached by the AR core plasma. Therefore, while in principle the results of Mitra-Kraev & Del Zanna (2019) are not necessarily surprising, the authors presented the event as a test-case, which they find to be representative of several microflares not reaching high temperatures. We note that "nanoflares" and "microflares" generally refer to coronal heating events with total energy of the order of $\sim 10^{24}$ and $\sim 10^{27}$ erg, respectively; in practice, the term "microflare" is often used loosely, and applied to heating events of GOES class A,B, or of lower energy.

In this paper we carry out a new analysis of the same event presented by Mitra-Kraev & Del Zanna (2019) and find that the observations point to significantly larger peak coronal temperatures (∼10 MK) than derived by Mitra-Kraev & Del Zanna (2019). As we detail in the rest of the paper, the main reason for the discrepancy between our results and those presented by Mitra-Kraev & Del Zanna (2019) is that Mitra-Kraev & Del Zanna (2019) appear to have neglected the initial phases of this heating event, when the temperature reaches its highest values, and the AIA observations in the 131 Å channel, which is most sensitive to ∼10 MK plasma.

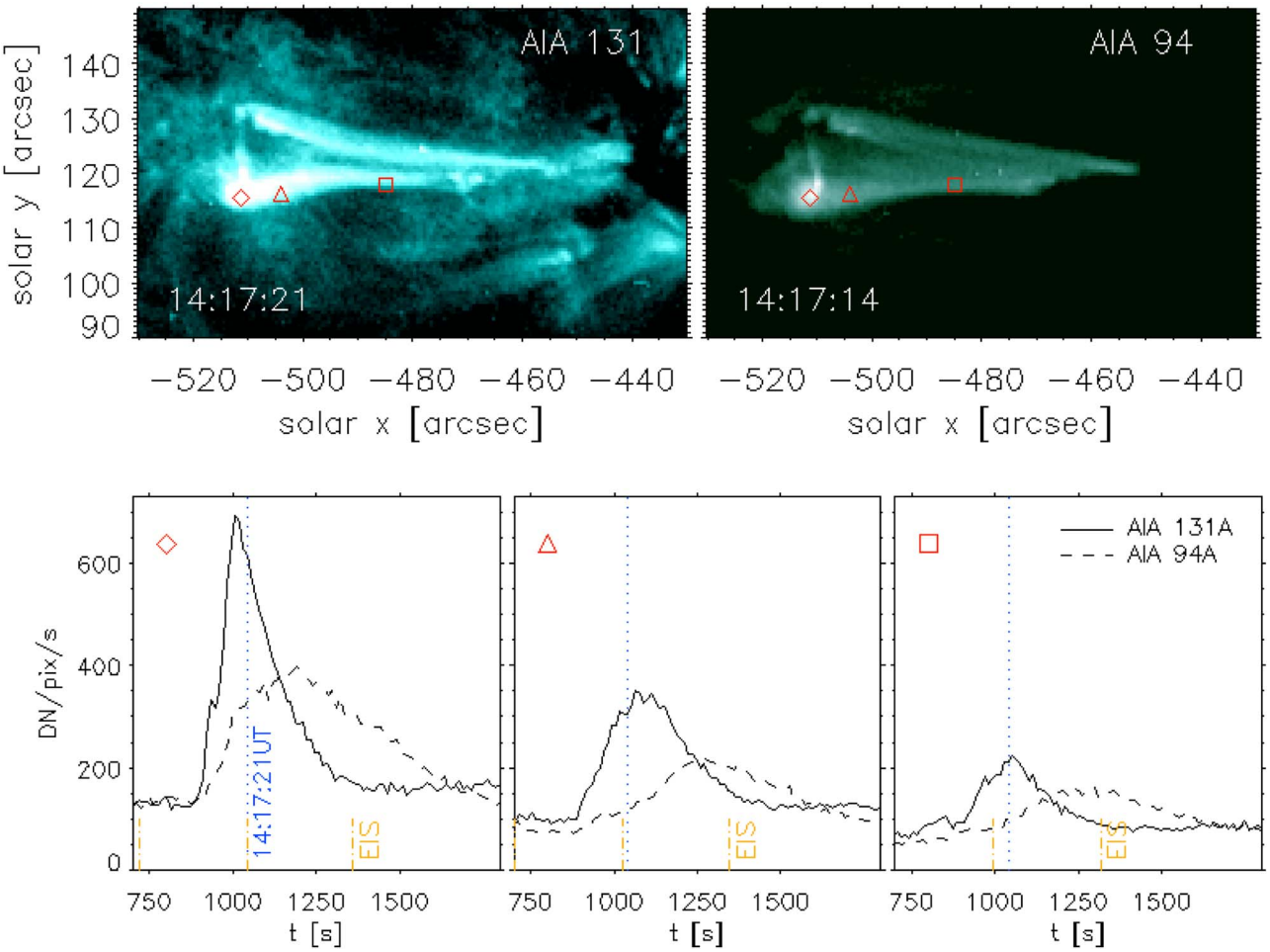

Figure 1. Upper row: AIA observations in the 131 Å (left) and 94 Å (right) passbands of transient hot loops observed in AR 11283 on 2011 September 3. We show images at a time in the initial phase of the heating event, when hot loops are clearly visible in the 131 Å passband. Bottom row: light curves of AIA 131 Å (solid) and 94 Å (dashed) emission for three locations along the hot loops, as marked in the top panel with the corresponding symbols. The reference time (i.e., $t = 0$) is 14UT on 2011 September 3. The vertical dotted blue line marks the time corresponding to the 131 Å image of the top left panel. We also indicate, with orange dashed–dotted lines, the approximate times where the Hinode/EIS slit overlaps with the selected three locations, in three consecutive rasters (see the text and Figure 4 for further details); note that EIS scans the region from W to E therefore within each raster the slit (which is oriented in the N–S direction) overlaps first the location marked by the square, then the triangle, and then the diamond.

2. Observations and Data Analysis

The event we study occurred in AR 11283 on 2011 September 3, around 14:17UT. Here we mostly focus on observations taken with SDO/AIA and with Extreme-Ultraviolet Imaging Spectrometer (EIS; Culhane et al. 2007) on board Hinode (Kosugi et al. 2007). The AIA coronal imaging data we analyze are observed in six narrow extreme ultraviolet (EUV) channels (94, 131, 171, 193, 211, 335 Å), which are characterized by 0.″6 pixels, and 12 s cadence and sample the transition region and corona across a broad temperature range (Boerner et al. 2012, 2014). We use AIA level 1.5 data, which have been processed for the removal of bad-pixels, despiked, flat-fielded, and image registered (coalignment among the channels, with adjustment of the roll angle and plate scales; Lemen et al. 2012).

The Hinode/EIS rasters we analyze (study acronym HH_Flare+AR_180x152) use the 2″ slit, 9 s exposure time at each slit position, and raster steps of 6″. The raster cadence of the EIS observations is about 5 minutes. The Hinode/EIS data sets were reduced using standard routines available in the Hinode/EIS branch of Solar Software (Freeland & Handy 1998).

Most of the observations of these events are also described in detail by Mitra-Kraev & Del Zanna (2019). However, besides the data analyzed by Mitra-Kraev & Del Zanna (2019), we also analyze a few additional data sets. In particular, for Hinode/EIS, while Mitra-Kraev & Del Zanna (2019) only consider the raster starting at 14:19:22 (as well as a raster about 30 minutes before the event), here we also analyze the two EIS rasters (14:08:40–14:13:49, and 14:14:01–14:19:09), preceding the one starting at 14:19:22, because they cover the very early phases of the event. For AIA, we also analyze the emission observed in the 131 Å passband, which was not considered by Mitra-Kraev & Del Zanna (2019). The AIA 131 Å passband provides very important temperature constraints as it includes strong emission from highly ionized Fe (especially from Fe XXI; e.g., Martínez-Sykora et al. 2011; Boerner et al. 2014)

In Figure 1 we show the images of the hot transient loops as observed in the AIA 131 and 94 Å passband, around 14:17UT. We also show the light curves in the 131 and 94 Å AIA passbands at three different locations along the hot loops. The

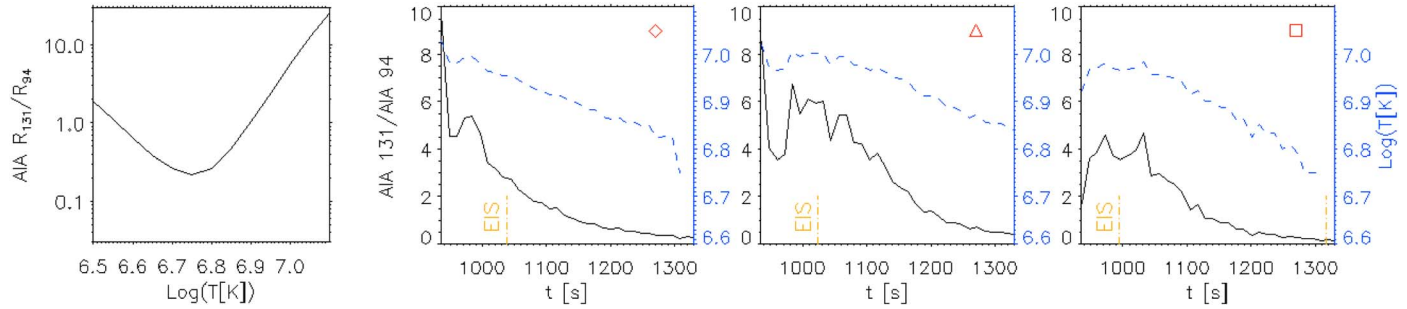

Figure 2. Left panel: AIA 131 Å/94 Å filter ratio, in the 6.5–7.1 Log $T[K]$ range obtained from the ratio of the AIA response functions in the 131 and 94 Å passbands. Panels 2–4: Measured ratio (black solid lines) of the background subtracted 131 and 94 Å emission at three different locations along the hot loops, as a function of time (see bottom row of Figure 1 and the main text). In each plot we also show the derived Log $T[K]$ (blue dashed line; corresponding scale is on the right axes), assuming the temperature is on the higher temperature branch of the ratio diagnostics of the left panel (i.e., Log $T[K] \geqslant 6.75$). As in Figure 1, the orange dashed–dotted lines indicate approximate times at which the Hinode/EIS slit overlaps with the selected three locations.

light curves show a significant increase of the emission in the hotter 131 Å passband preceding the increase in the 94 Å passband, pointing to a fast increase in coronal temperature in the early phases of the heating event, followed by cooling, which in turn causes a decrease in the 131 Å emission and an increase in the cooler 94 Å emission. We can obtain a first rough estimate of the coronal temperatures in the observed heating event by using a filter ratio diagnostic via the 131 Å/94 Å ratio (see the left panel of Figure 2). In Figure 2 we show the measured ratios of the background subtracted 131 and 94 Å emission at the three locations marked in Figure 1. For all pixels, the "background" emission we subtract is the emission in that given pixel at $t = 756$ (i.e., ∼14:12:36UT; see Figure 1). We plot the ratios starting from $t = 936$ (i.e., ∼14:15:36UT) as before that time the 94 Å (background subtracted) emission is essentially zero. The peak ratios have values between ∼4 and 10, corresponding to temperatures of 9.5–10.5 MK. The filter ratio of course provide only a crude estimate of the temperature, under the isothermal assumption; therefore, in order to take into account the full information from the AIA observations in its six coronal EUV passbands (94, 131, 171, 193, 211, 335 Å) we also derived an emission measure distribution, using the inversion method of Cheung et al. (2015). The observed emission in the AIA narrowband EUV channels (I_i, for the passband i, in units of DN s^{-1} pix^{-1}) depends on the thermal properties of the optically thin coronal plasma in the pixel, as $I_i = \int_T R_i(T)\ \mathrm{DEM}(T)\ dT$, where $R_i(T)$ is the response function in a given passband (in units of DN cm^5 s^{-1} pix^{-1}), and the differential emission measure (in units of cm^{-5} K^{-1}) is defined by $\mathrm{DEM}(T)\ dT = \int_z n_e^2(T)\ dz$, where $n_e(T)$ is the electron density of the plasma at temperature T. We then obtain the distribution of emission measure (EM(T), in units of cm^{-5}) as a function of temperature by integrating the DEM(T) over ΔLog $T[K]$ (which is 0.1 in our case). In Figure 3 we show the spatial maps of the hot EM at three times, as well as the temporal evolution of the EM(T) at the three locations marked in Figure 1. These results show the presence of significant hot emission around 10 MK, especially close to the eastern footpoint of the loop. We note that Mitra-Kraev & Del Zanna (2019) derive a plasma temperature of ∼5 MK around 14:22–14:23 (corresponding to 1320–1380 s in our plots, which assume a reference time of 14UT), from data averaged over a large region including the western loop leg (see, e.g., their Figures 11–12), where we selected one of the pixels for our analysis (marked by a square in Figures 1–3). At that time, the 131 Å emission in that region is already negligible (see the bottom right panel of Figure 1), so the filter ratio diagnostics will have large uncertainties. However, our DEM results shown in Figure 3 show that around that time and for that location, the DEM has a peak around Log $T[K] \sim 6.75$ (which is compatible with the temporal evolution of the temperature diagnosed through the filter ratio; see rightmost panel of Figure 2), in good agreement with the DEM results of Mitra-Kraev & Del Zanna (2019) shown in their Figure 12, although they are averaging over a large area, so no direct detailed comparison should be made.

We then analyzed the Hinode EIS spectral observations, in particular, focusing on the three rasters covering the early phases of the microflare (starting at 14:08:40, 14:14:01, and 14:19:22). In Figure 4 (top panels) we show maps of the intensity integrated in two small wavelength ranges (10 spectral pixels) centered on the Fe XVII 254.88 Å (left column) and Fe XXIII 263.76 Å (right column) emission line, respectively. The Fe XXIII intensity map shows an excess, close to the loop footpoint, only in the second raster (14:14:01–14:19:09), so we extracted the spectra to investigate in more detail the constraints on the Fe XXIII emission. In the bottom panel of Figure 4 we show the EIS spectrum (in units of DN/s) in the spectral window containing the Fe XXIII 263.76 Å line, averaged over 6 pixels in the N–S direction (i.e., along the slit, and therefore in the same time step at 14:17:23) to improve the signal-to-noise. Although the spectrum is still rather noisy there is a spectral feature that appears to be compatible with it being Fe XXIII emission. We performed a fit with a function including a constant background, and two Gaussians: one for the Fe XXIII line and the other one to take into account a narrow spectral feature observed around 263.5 Å (also observed by, e.g., Polito et al. 2018a, see their Figure 6, in flare observations). The parameters of the best fit indicate for the Fe XXIII line a blueshift of about 70 km s^{-1}, and a $(1/e)$ nonthermal broadening of the order of 40 km s^{-1}. These values seem reasonable for a microflare, and we will discuss them further in the following sections, which are dedicated to the hydrodynamic modeling of this event, and the overall discussion. For a cross-check between AIA and Hinode/EIS we also calculated the 131 and 94 Å AIA emission predicted, under isothermal assumptions, on the basis of the measured Fe XXIII emission. In Figure 5 we show the predicted curves, as a function of temperature, and compare them with the observed values at the same time, and approximately the same location (we use the values of the easternmost pixel, marked by a

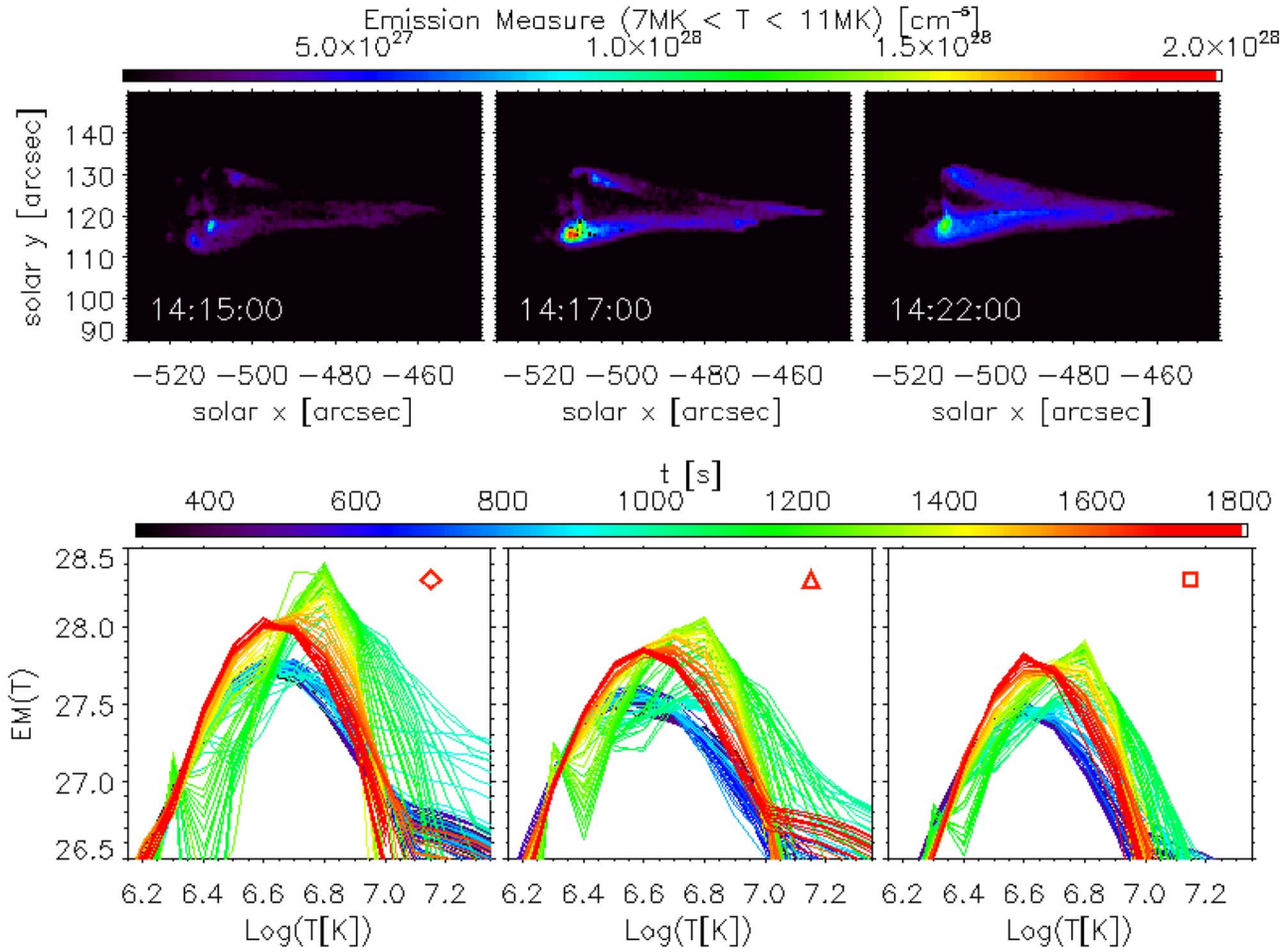

Figure 3. Thermal analysis of the AIA observations of the microflare. Top row: spatial distribution of the hot emission (EM(T) integrated in the 7–11 MK temperature range) at three different times before/at/after the peak. Bottom row: temporal evolution of the EM(T) at the three locations along the hot loops marked in Figure 1 with the corresponding symbols.

diamond, of Figures 1–3). We find a very good agreement between the AIA and Hinode/EIS measurements (within ∼0.025 in $\Delta \mathrm{Log}T[K]$, between the 131 Å and the 94 Å channels).

Therefore, we conclude that the results of our analysis of this microflare are overall in agreement with the findings of Mitra-Kraev & Del Zanna (2019), although our conclusions are rather different, and pointing to significantly larger peak temperatures for this event, because they only analyzed the decay phase of the microflare and therefore missed the hotter initial phase.

3. Hydrodynamic Loop Modeling

As a further aid to the interpretation of data we performed forward modeling with hydrodynamic simulations of impulsively heated loops. We considered a standard model of a single semicircular loop symmetric with respect to the apex (see Reale et al. 2019a for a recent application and references therein). Plasma flows and energy transport occur exclusively along the field lines, i.e., along the loop, which stands vertical on the solar surface. The model includes the detailed physical effects for magnetically confined plasma, and in particular curvilinear gravity, thermal conduction, radiative losses from optically thin plasma, compressional viscosity, and plasma ionization. From the distance of the footpoints, as observed in AIA, we estimated a loop half-length of 35 Mm, but we also considered the possibility of a more elongated loop with half-length of 40 Mm. The hydrodynamic equations for a compressible plasma are solved numerically (Peres et al. 1982) with adaptive mesh refinement (Betta et al. 1997). A steady heating term keeps the initial loop in equilibrium.

The model describes the evolution of the plasma of a complete loop atmosphere from the chromosphere to the corona, through the steep transition region. We considered an initial unperturbed atmosphere with a maximum temperature of ∼2 MK and a pressure ∼0.6 dyne cm^{-2}, corresponding to a density of $\sim 1 \times 10^9$ cm^{-3}, chosen such that it is much cooler and more tenuous than after the heat pulse, but also able to provide enough plasma reservoir to fill the heated loop.

The heat pulse is described as a function with a separate dependence on time and space. The time-dependence is a simple top-hat function. We considered two values for duration: 2 and 3 minutes. We also considered two possible locations for the heat pulse, one is a uniform spatial distribution in the corona (the efficient thermal conduction makes any specific location in the corona practically equivalent Reale et al. 2019b), the other is a narrow Gaussian (1 Mm wide) just above the transition region, i.e., two twin pulses localized at the loop footpoints. The heat pulse intensity is in the range between 1×10^9 and 5×10^9 erg cm^{-2} s^{-1}, enough to bring the loop plasma to temperatures around 10 MK.

The simulations provide the evolution of the density, velocity, and temperature (and pressure) of the plasma confined

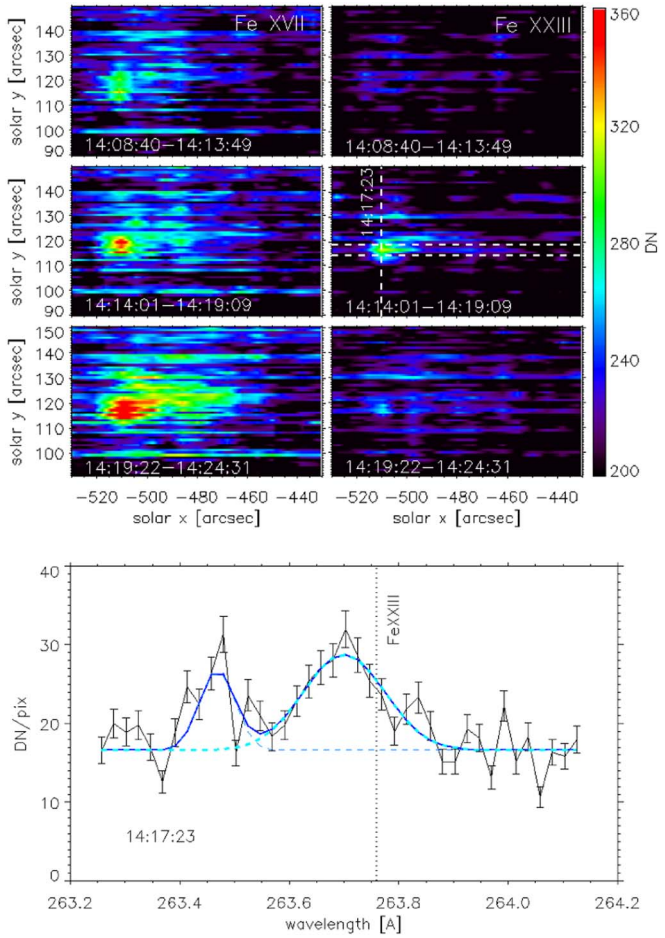

Figure 4. Top panels: spectroheliograms in two different spectral lines, Fe XVII 254.88 Å (left column) and Fe XXIII 263.76 Å (right column), for the three consecutive rasters (one for each row) taken during the initial phases of the microflare. We show a portion of the EIS field of view centered around the region of interest where the microflare occurs. The vertical dashed line in the Fe XXIII intensity map for the second raster (i.e., second panel from the top in the right column) marks the timestep for which we show, in the bottom panel, a spectrum averaged over the pixels between the two horizontal dashed lines). Bottom panel: Hinode EIS spectral observations around the Fe XXIII 263 Å spectral line, at the loop footpoint and averaged over six spatial pixels (in the y direction, i.e., along the slit we selected adjacent pixels at the same time step, at $t = 14:17:23$), as marked by the dashed lines in the top figure (second panel from the top in the right column). The vertical dotted line indicates the rest wavelength of the Fe XXIII line, the cyan lines show the two Gaussian components of the fit, while the blue line indicates the total best-fit function.

in the half-loop. From them we synthesize the emission to be compared with the one observed with SDO/AIA and Hinode/EIS. For AIA we use the standard temperature response function extracted from SSW for the date of the observation, in particular for the 94 and 131 Å channels. For EIS we use the CHIANTI emissivity for the Fe XXIII line calculated using CHIANTI 9 (Dere et al. 2019) with the CHIANTI ionization equilibrium. The best agreement with measured intensities is obtained by assuming element abundances intermediate between the photospheric (e.g., Grevesse & Sauval 1998) and coronal abundances (e.g., Feldman 1992). We note that this is in good agreement with several observations of impulsive events (from microflares to larger flares), which often point to coronal abundances in flares being lower than typically observed in nonflaring active regions, and closer to photospheric (e.g., Warren et al. 2016a; see also review of Testa 2010 and references therein).

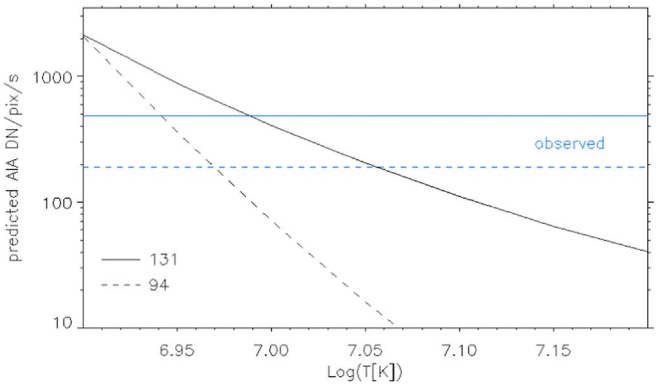

Figure 5. AIA 131 and 94 Å emission predicted (black curves) by using the Fe XXIII emission measured by Hinode EIS at 14:17:23 (see the bottom panel of Figure 4), and taking into account the Fe XXIII emissivity curve and the AIA responses as a function of temperature. The horizontal curves in blue represent the measured AIA 131 Å (solid) and 94 Å (dashed) emission at the loop footpoint (location marked by the diamond in Figures 1–3).

Table 1
Parameters of the Hydrodynamic Loop Simulations in Figures 6–8

Label	Half-length (Mm)	Heat Flux (10^9 erg cm^{-2} s^{-1})	Heat Duration (s)	Heat Location
A	35	1.4	180	corona
B	35	1.3	180	footpoints

In the following we show sample results that provide a good match with the observations, and in particular for two simulations for which the parameters are listed in Table 1. As usual for time-dependent model-data comparisons, and given the relatively simplified single-loop modeling, we do not necessarily expect a perfect fit of the observations, but a general qualitative/quantitative matching. The comparison is made with the emission detected in the pixels marked in Figure 1.

Figure 6 shows results for a simulation of a loop with half-length 35 Mm heated by a pulse, with a duration of 3 minutes, uniformly deposited in the loop corona (simulation A in Table 1). Each column of Figure 6 pertains to a different loop segment, selected for comparison with the emission in each pixel marked in Figure 1. From Figure 1 it is clear that the loop is not seen face-on but from above and, since the loop is located not too close to disk center, and closer to the E limb, we see the left (E) leg mostly compressed within a few pixels, likely contributing to its brighter emission compared to the W footpoint. To account for this effect for comparison with the leftward pixels we integrate over loop segments of several pixels, much less for the rightmost one, which is in the right leg.

Focusing on the left column, i.e., the one related to the easternmost pixel, the temperature and density show the usual flare evolution, a fast rise for temperature, tracing the heat pulse duration, and more gradual for density, tracing the loop filling with plasma coming up from the chromosphere, with the velocities shown in the second panel. The temperature peaks at ~12 MK, with a plateau of ~3 minutes, and decays down to ~3 MK in ~800 s. The density reaches its peak ~2×10^{10} cm^{-3} about 3 minutes later than the temperature and decays much more gradually thereafter. This temperature/density

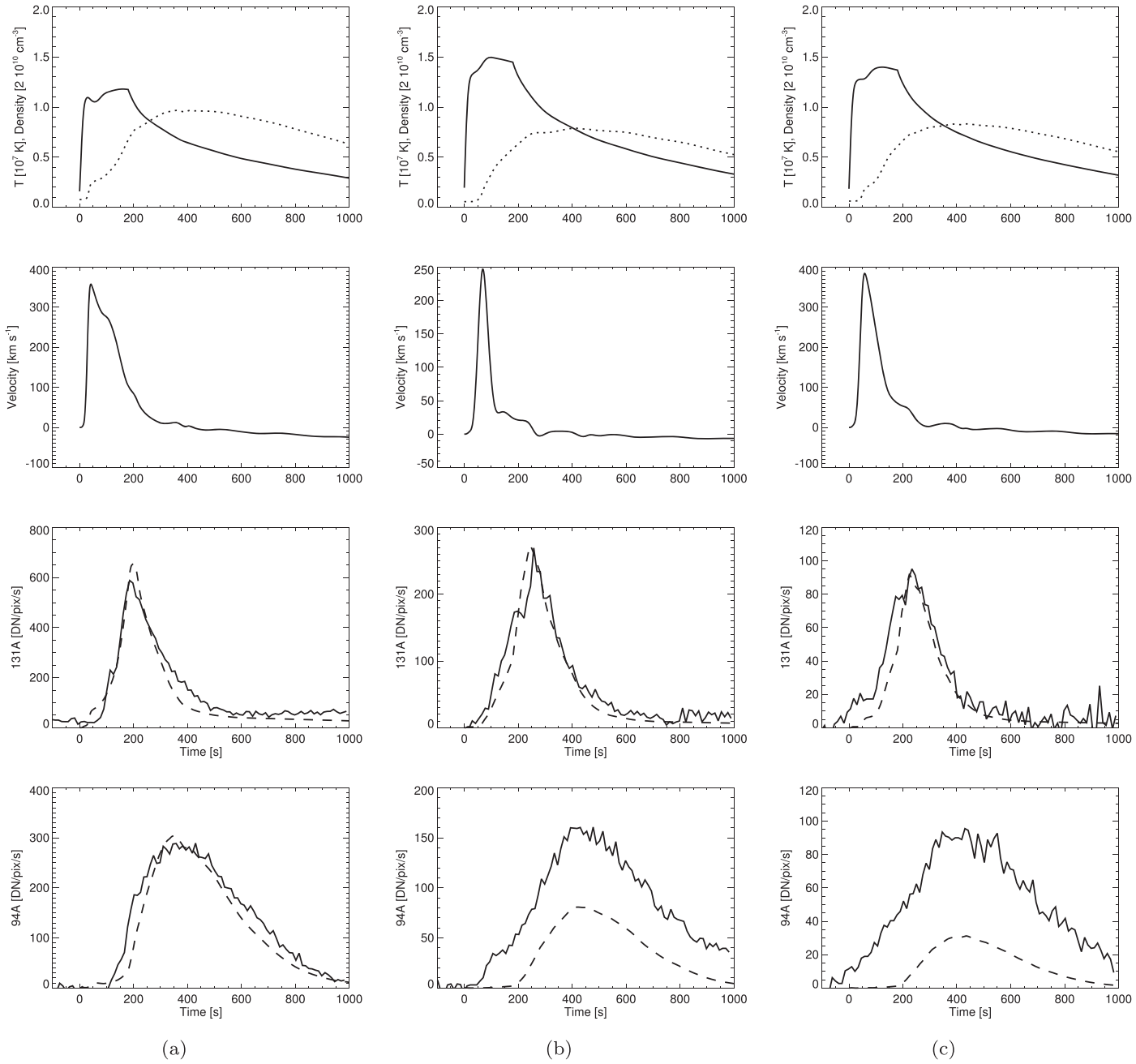

Figure 6. (a) Temperature (solid) and density (dotted, upper panel), velocity (second panel), and emission in the 131 Å (dashed line, third panel) and in the 94 Å (bottom panel) from the hydrodynamic loop simulation with a heat pulse deposited in the loop corona (simulation A in Table 1) averaged over a loop segment between 10 and 14 Mm from the loop base, compared to the emission detected in the leftmost pixel marked in Figure 1 (solid lines). (b) Same as (a) averaged over a loop segment between 28 and 30 Mm from the loop base, compared to the emission detected in the middle pixel marked in Figure 1. (c) Same as (a) averaged over a loop segment between 20.0 and 20.7 Mm from the loop base, compared to the emission detected in the rightmost pixel marked in Figure 1.

evolution determines the emission in the 131 Å and 94 Å channels shown in the lowest two panels (dashed lines). In the 131 Å channel the emission lasts for a short time (∼5 minutes) and has a sharp peak at time $t \approx 200$ s, i.e., at a temperature of ∼10 MK and a density close to the peak value. In the 94 Å channel the brightening is delayed and more gradual, lasting about 10 minutes and with a smooth peak at time $t \approx 400$ s. The modeled emission matches well the observations in terms of intensity, shape, and timing, in both channels, including the relative timing.

The second and third columns of Figure 6 show results of different segments of the loop for comparison with the middle and right pixels of Figure 1. The segments are taken higher along the loop, which corresponds to a higher temperature (∼15 MK), than in the left column. The lower density, together with the smaller length of the segments, explains the overall lower emission rate from the pixels. For these other two pixels the model still matches well the observed shape and the timing. At variance from the first pixel, here we find that while we match well the intensity in the 131 Å channel, we underestimate the one in the 94 Å channel by a factor of 2–3. We explain this discrepancy by noting that, most likely, our single loop model does not entirely describe the observed loop. In particular, we expect that the heat pulse has a shaped

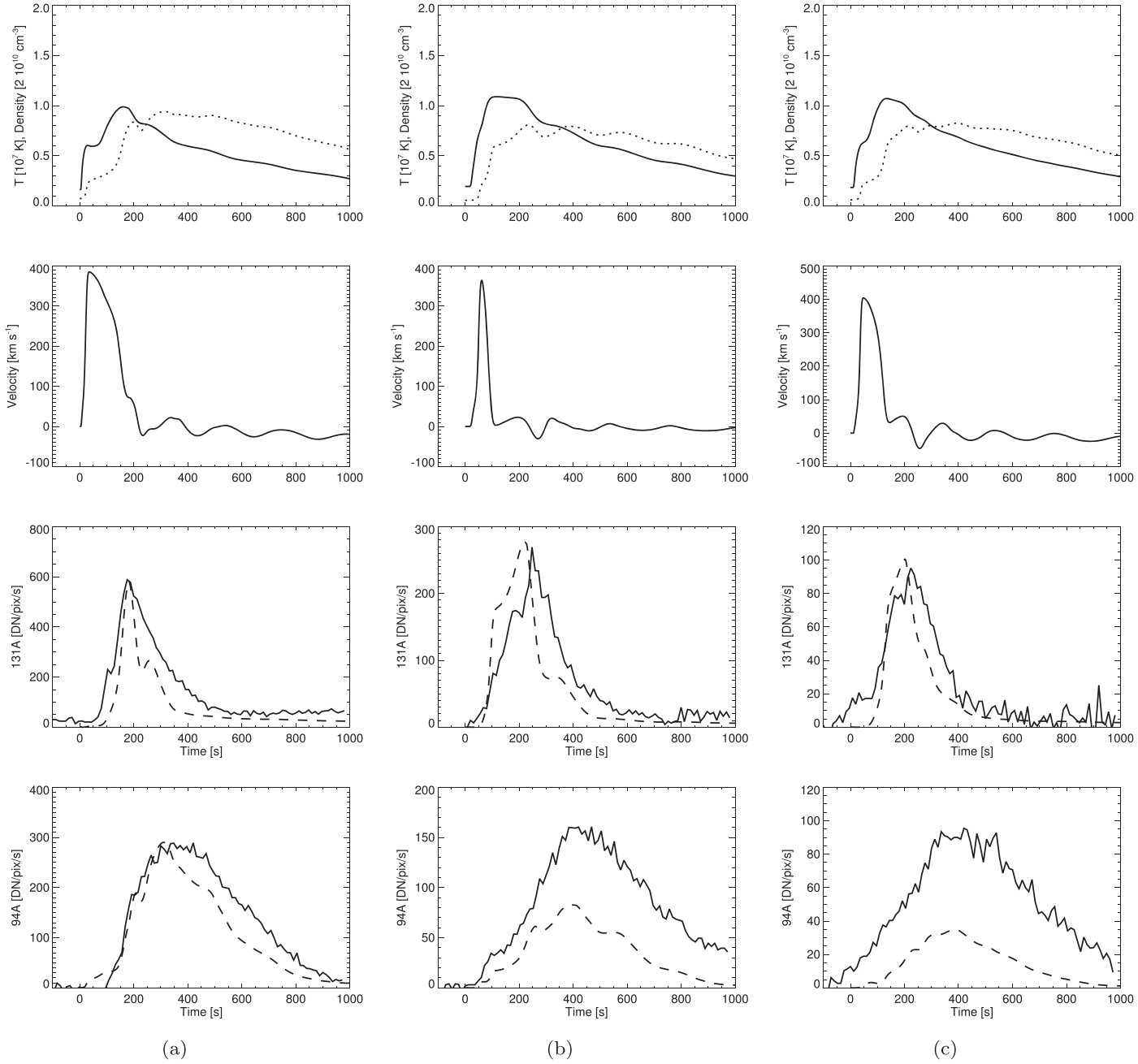

Figure 7. Same as Figure 6 for a heat pulse deposited at the loop footpoints (simulation B in Table 1). The quantities are averaged over a loop segment between 10 and 15 Mm, 28 and 30 Mm, and 20.0 and 20.8 Mm, respectively, from the loop base.

distribution across the loop, and therefore, a smaller rate in the tail corresponds to loop shells heated to lower temperatures. In turn, this corresponds to an emission excess in the 94 Å channel, not explained by the single loop model. We see this effect higher in the loop, which is observed more "face-on" than at the E footpoint.

Figure 7 shows the results from another model (simulation B of Table 1) with a heat pulse located at the footpoints. For the footpoint-heated case we have a lower peak temperature, and a comparable peak density ($\sim 2 \times 10^{10}$ cm^{-3}). In this case, the heat pulse triggers a sloshing wave (as in Reale 2016), with well defined density and velocity pulsations. These pulsations determine a clear second bump in the left light curve of the 131 Å channel, which does not appear in the observed light curve. We also notice a faster evolution of the emission in the 94 Å channel, less in agreement with the observed light curve. The agreement is less good also regarding the timing of the other two light curves of the 131 Å channel, which precede the observed one.

To complete our diagnostic scenario we compare Fe XXIII line profiles synthesized from our simulations to the Hinode/EIS observations. Figure 8 shows this comparison for the two simulations shown in Figures 6 and 7. Each upper panel includes 7 profiles taken at different times around the peak of the corresponding light curve, shown in the lower panel, for comparison with the observed one (data points). Each profile is integrated over exactly the same loop segment as the one used for the left pixel of Figure 1, and a good matching with the

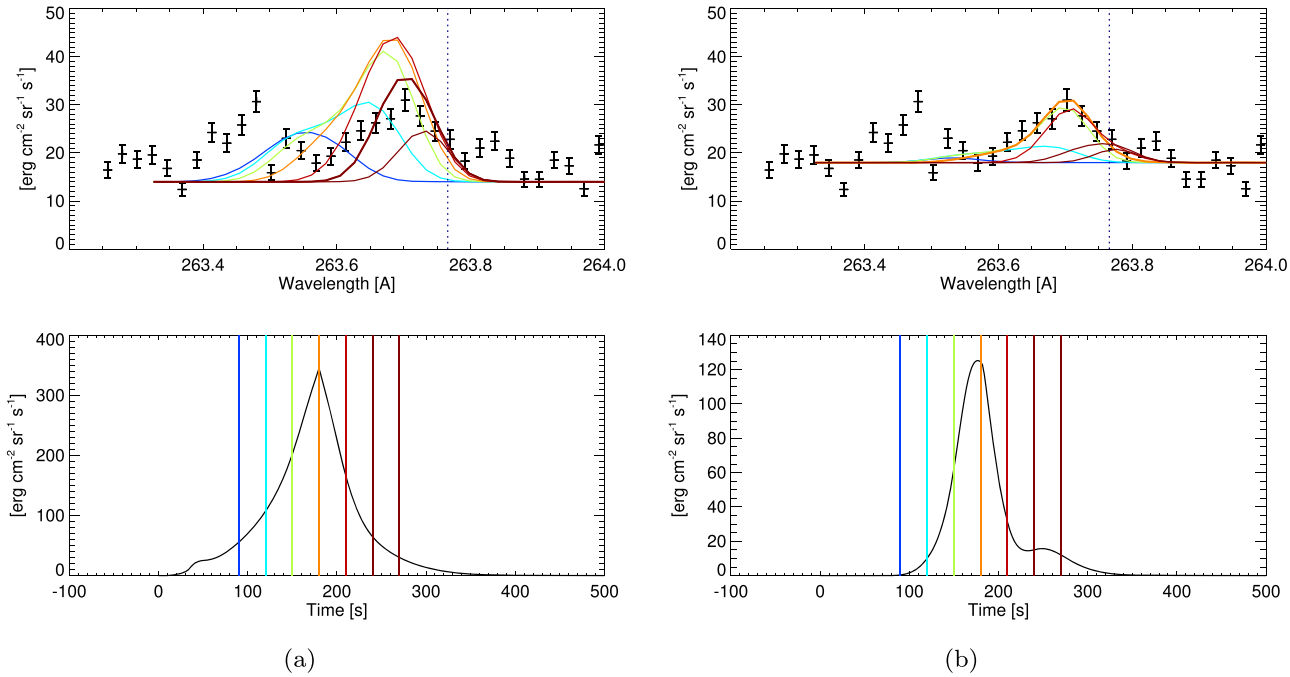

Figure 8. (a) Profiles (upper panel) and light curve (lower panel) in the Fe XXIII line for simulation A. The respective times of the line profiles are marked in the light curve. The line profiles are averaged over 120 s centered at these times. The observed line profile is also shown with error bars, and the best matching profile is marked (thicker line). (b) Same as (a) for simulation B, averaged over 90 s.

observed line width is obtained by averaging over 120 s and 90 s, respectively. If we average over 9 s, we still obtain the correct line shift and total intensity, but the line is considerably less broad. This is additional evidence that the loop is probably multistructured and that the evolution of the substrands is slightly time-shifted from one to another, thus contributing slightly different shifts to the total observed line (see, e.g., Polito et al. 2019). We do not apply any normalization, we only add an offset (analogous to the constant included in the fitting of the EIS spectrum; see Section 2) of 14 and 18 erg cm^{-2} r^{-1} s^{-1}, respectively. The upper panels of Figure 8 show that, around the emission peak, the line from the simulations is broad and strongly blueshifted, according to the strong upflows shown by the velocities of Figures 6 and 7. The blueshift decreases with time. Also the observed profile is broad and blueshifted, and for each model we find one profile that closely resembles the observed one (red in (a), orange in (b)). The agreement, both for width and for shift, is good for both simulations, and slightly better for the footpoint heat pulse (simulation B), although the time of the best profile is closer to the observed one for the coronal heat pulse (simulation A).

4. Discussion and Conclusions

In this paper we have analyzed coronal imaging (AIA) and spectral (Hinode/EIS) observations of a solar microflare, in particular focusing on the high temperature emission during the heating event. This event had been previously partly analyzed by Mitra-Kraev & Del Zanna (2019), who had presented it as a test-case study of a class of microflares reaching only low peak temperatures ($\lesssim$5 MK).

A range of peak temperatures for microflares is certainly plausible, and recent observations of some events possibly point to particularly low temperatures; for instance, Hannah et al. (2019) derive for a microflare observed with NuSTAR a temperature of $\sim$5 MK, though from an isothermal fit, and very short integration time of $\sim$3 s; and, similarly, Cooper et al. (2020) find for a different microflare a temperature of $\sim$6.7 MK, with an isothermal assumption and integration time of $\sim$15 s. However, the results of Mitra-Kraev & Del Zanna (2019) is quite intriguing given, for instance, the significant emission in hot channels such as the AIA 94 Å passband and the Hinode XRT filters. This spurred us to revisit the data and investigate in detail the available temperature diagnostics.

Our analysis includes the initial phase of the microflare, not analyzed by Mitra-Kraev & Del Zanna (2019), and indicates a peak plasma temperature $\gtrsim$10 MK, similar to what we observed in a sample of a dozen microflares observed by AIA (Reale et al. 2019a; Testa et al. 2020) and other studies have also found by using X-ray observations (see, e.g., Hannah et al. 2011 and references therein). The detection of Fe XXIII emission, although weak, in Hinode/EIS spectral observations is of particular interest as it is only seldom observed in small heating events (e.g., Del Zanna 2008; Madjarska 2011; Mulay et al. 2018). Several elements of our analysis point to the high peak temperature of this heating event: (1) the AIA emission in different passbands and its evolution (we apply both a simple filter ratio technique and a DEM inversion); (2) the likely presence of Fe XXIII emission in the Hinode/EIS spectral observations; (3) the 1D loop modeling, which finds a good agreement with the observations for a flaring loop reaching temperatures $\sim$10–15 MK. Indeed, we find that a single loop model can provide a good match to several observed properties, including the AIA intensities and temporal variability at three locations along the loop, and the Hinode/EIS Fe XXIII line profile. The model provides a good quantitative match, including accurate timing (in each AIA band, between the 131 and 94 Å AIA passbands, and between AIA and the EIS Fe XXIII observations), as well as the Fe XXIII line shift and width, without the need of normalization. In agreement with Mitra-Kraev & Del Zanna (2019), we find that abundances

lower than coronal and closer to photospheric yield a better agreement between models and observations. The hydrodynamic loop modeling of this event also allows us to infer constraints on the properties of the heating, and in particular (1) the pulse intensity (a flux $\sim 10^9$ erg cm^{-2} s^{-1}, which corresponds to a rate $\sim 6 \times 10^{24}$ erg s^{-1}, if we assume a circular loop cross-section with a radius of 0.″6 [AIA pixel], or $\sim 10^{25}$ erg/s if we assume the radius to be 550 km as from Brooks et al. 2012; Aschwanden & Peter 2017; Williams et al. 2020); (2) the pulse duration (∼2–3 minutes), corresponding to a total injected energy $\sim 10^{27}$ erg.

The location of the energy release is not conclusively determined by the comparison with the simulations: the light curves and the timing of the Fe XXIII line profiles seem to slightly favor the heating in the corona, whereas the shape of the line profiles themselves are better matched by the footpoint heating.

Heating at a single footpoint would also be an interesting scenario to consider because emergence of flux and reconnection at one footpoint has been proposed to explain similar observations with hot Fe XXIII footpoints (e.g., Mulay et al. 2018). However, our symmetric model is able to consistently explain the asymmetric appearance of the loop brightness, due to the geometry. The model light curves shown in Figures 6 and 7 are obtained by integrating on longer loop segments on the western side of the loop: we see a much brighter left footpoint because, due to perspective, the left leg is squeezed over a few pixels, while the right leg is not. We checked that even the footpoint-heated model does not lead to bright footpoints in the Fe XXIII line at any time during the simulated evolution, and instead it produces a line that is intense in the higher parts of the loop, where the temperature is higher. We also note that in general there is little correspondence between the location of the heating and the brightness distribution in EUV and X-ray emission because the plasma emission is determined by a combination of temperature and density evolution, and the latter is determined by pressure gradients that are not directly linked to heating deposition (e.g., Reale et al. 2000).

In addition, our loop modeling points to a heating release probably structured across the loop. The model reproduces only partly the 94 Å emission high in the loop, thus strongly suggesting the presence of other lower intensity heating along the line of sight, probably in shells outside of the central core. The observed broad Fe XXIII line probably also indicates a structured heating because it is reproduced by averaging the model in time, which means that the overall observed evolution is the result of an ensemble of heating events slightly shifted in time. This is not surprising, and a similar effect has been pointed out in other flare events (Reale et al. 2012; Warren et al. 2013).

The results presented here, pointing to high temperatures (∼10 MK) in small heating events, fit well in a scenario, supported by several recent studies (e.g., Testa et al. 2014; Warren et al. 2016b; Reale et al. 2019a, 2019b; Glesener et al. 2020), in which small heating events (down to ∼nanoflare-size events) appear to have similar characteristics to larger flares, such as high plasma temperatures and particle acceleration. At the lower energy end of this class of events it is generally difficult to directly detect emission from nonthermal particles resulting from acceleration caused by the reconnection process (see, e.g., Testa et al. 2014; Hannah et al. 2016; James et al. 2017; Wright et al. 2017; James & Subramanian 2018; Hannah et al. 2019). Spectral observations of the transient brightenings at the footpoints (chromosphere and transition region) of heated loops with the Interface Region Imaging Spectrograph (IRIS; De Pontieu et al. 2014), combined with 1D RADYN (Carlsson & Stein 1997; Allred et al. 2015) modeling of nanoflare-heated loops, provide indirect evidence of the presence of nonthermal particles in small heating events (Testa et al. 2014, 2020; Polito et al. 2018b). In Testa et al. (2020) we studied a sample of heating events with a broad range of overall energy and loop sizes, all with rapid transition region brightenings associated with the coronal heating, and we find very similar coronal morphology suggesting they might be driven by large angle reconnection (Reale et al. 2019a). We also find spectral signatures of heating by accelerated particles even in some of the smallest events (Testa et al. 2020).

In the last few years, despite some technical challenges in observing solar active regions (e.g., Hannah et al. 2016, 2019), direct imaging of solar hard X-ray emission using the astrophysical observatory NuSTAR (Harrison et al. 2013) has allowed us to push down detection limits of previous observations with RHESSI (Lin et al. 2002), and it has provided new constraints on the nonthermal emission in small heating events in the solar corona. These recent NuSTAR observations (e.g., Wright et al. 2017; Cooper et al. 2020; Glesener et al. 2020) are in good agreement with the constraints on nonthermal particles we derive from our observations and modeling of chromospheric and transition region response impulsive events. In particular, our IRIS analyses suggest a variety of distributions of nonthermal particles, even in a single event, with generally small low-energy cutoff ($E_c \sim$ 5–15 keV) and steep slopes (electron spectral index $\delta \sim 7$), in agreement with the recent findings of Wright et al. (2017), Glesener et al. (2020), and Cooper et al. (2020). Further multi-instrument observations of small-scale nano/microflare events (e.g., Hannah et al. 2019) will help constrain even more the connection between particle acceleration and heating in active regions outside large flares.

We thank Vanessa Polito for useful discussions regarding the analysis of Hinode/EIS data. We thank the anonymous referee for useful suggestions that have helped improve the paper. P.T. was funded for this work by the NASA Heliophysics Guest Investigator grant NNX15AF50G. P.T. was also supported by contracts 8100002705 and SP02H1701R from Lockheed-Martin to SAO, and NASA contract NNM07AB07C to the Smithsonian Astrophysical Observatory. F.R. acknowledges support from Italian Ministero dell'Università e della Ricerca and financial contribution from the Agreement ASI-INAF n.2018-16-HH.0. This research has made use of NASA's Astrophysics Data System and of the SolarSoft package for IDL. Hinode is a Japanese mission developed and launched by ISAS/JAXA, with NAOJ as a domestic partner and NASA and STFC (UK) as international partners. It is operated by these agencies in cooperation with the ESA and NSC (Norway). SDO data were obtained courtesy of NASA/SDO and the AIA and HMI science teams.

ORCID iDs

Paola Testa https://orcid.org/0000-0002-0405-0668
Fabio Reale https://orcid.org/0000-0002-1820-4824

References

Allred, J. C., Kowalski, A. F., & Carlsson, M. 2015, ApJ, 809, 104
Aschwanden, M. J., & Peter, H. 2017, ApJ, 840, 4
Barnes, W. T., Cargill, P. J., & Bradshaw, S. J. 2016, ApJ, 829, 31
Betta, R., Peres, G., Reale, F., & Serio, S. 1997, A&AS, 122, 585
Boerner, P., Edwards, C., Lemen, J., et al. 2012, SoPh, 275, 41
Boerner, P. F., Testa, P., Warren, H., Weber, M. A., & Schrijver, C. J. 2014, SoPh, 289, 2377
Brooks, D. H., Warren, H. P., & Ugarte-Urra, I. 2012, ApJL, 755, L33
Carlsson, M., & Stein, R. F. 1997, ApJ, 489, 159
Cheung, M. C. M., Boerner, P., Schrijver, C. J., et al. 2015, ApJ, 807, 143
Cooper, K., Hannah, I. G., Grefenstette, B. W., et al. 2020, ApJL, 893, L40
Culhane, J. L., Harra, L. K., James, A. M., et al. 2007, SoPh, 243, 19
De Pontieu, B., Title, A. M., Lemen, J. R., et al. 2014, SoPh, 289, 2733
Del Zanna, G. 2008, A&A, 481, L69
Del Zanna, G. 2013, A&A, 555, A47
Dere, K. P., Del Zanna, G., Young, P. R., Landi, E., & Sutherland, R. S. 2019, ApJS, 241, 22
Feldman, U. 1992, PhyS, 46, 202
Foster, A. R., & Testa, P. 2011, ApJL, 740, L52
Freeland, S. L., & Handy, B. N. 1998, SoPh, 182, 497
Glesener, L., Krucker, S., Duncan, J., et al. 2020, ApJL, 891, L34
Graham, D. R., De Pontieu, B., & Testa, P. 2019, ApJL, 880, L12
Grevesse, N., & Sauval, A. J. 1998, SSRv, 85, 161
Hannah, I. G., Grefenstette, B. W., Smith, D. M., et al. 2016, ApJL, 820, L14
Hannah, I. G., Hudson, H. S., Battaglia, M., et al. 2011, SSRv, 159, 263
Hannah, I. G., Kleint, L., Krucker, S., et al. 2019, ApJ, 881, 109
Harrison, F. A., Craig, W. W., Christensen, F. E., et al. 2013, ApJ, 770, 103
James, T., & Subramanian, P. 2018, MNRAS, 479, 1603
James, T., Subramanian, P., & Kontar, E. P. 2017, MNRAS, 471, 89
Klimchuk, J. A. 2006, SoPh, 234, 41
Kosugi, T., Matsuzaki, K., Sakao, T., et al. 2007, SoPh, 243, 3
Lemen, J. R., Title, A. M., Akin, D. J., et al. 2012, SoPh, 275, 17
Lin, R. P., Dennis, B. R., Hurford, G. J., et al. 2002, SoPh, 210, 3
Madjarska, M. S. 2011, A&A, 526, A19
Martínez-Sykora, J., De Pontieu, B., Testa, P., & Hansteen, V. 2011, ApJ, 743, 23
Mitra-Kraev, U., & Del Zanna, G. 2019, A&A, 628, A134
Mulay, S. M., Matthews, S., Hasegawa, T., et al. 2018, SoPh, 293, 160
Peres, G., Serio, S., Vaiana, G., & Rosner, R. 1982, ApJ, 252, 791
Pesnell, W. D., Thompson, B. J., & Chamberlin, P. C. 2012, SoPh, 275, 3
Polito, V., Dudík, J., Kašparová, J., et al. 2018a, ApJ, 864, 63
Polito, V., Testa, P., Allred, J., et al. 2018b, ApJ, 856, 178
Polito, V., Testa, P., & De Pontieu, B. 2019, ApJL, 879, L17
Reale, F. 2014, LRSP, 11, 4
Reale, F. 2016, ApJL, 826, L20
Reale, F., Guarrasi, M., Testa, P., et al. 2011, ApJL, 736, L16
Reale, F., Landi, E., & Orlando, S. 2012, ApJ, 746, 18
Reale, F., Peres, G., Serio, S., et al. 2000, ApJ, 535, 423
Reale, F., Testa, P., Petralia, A., & Graham, D. R. 2019a, ApJ, 882, 7
Reale, F., Testa, P., Petralia, A., & Kolotkov, D. Y. 2019b, ApJ, 884, 131
Teriaca, L., Warren, H. P., & Curdt, W. 2012, ApJL, 754, L40
Testa, P. 2010, PNAS, 107, 7158
Testa, P., De Pontieu, B., Allred, J., et al. 2014, Sci, 346, B315
Testa, P., De Pontieu, B., Martínez-Sykora, J., et al. 2013, ApJL, 770, L1
Testa, P., Drake, J. J., & Landi, E. 2012, ApJ, 745, 111
Testa, P., Polito, V., & Pontieu, B. D. 2020, ApJ, 889, 124
Testa, P., & Reale, F. 2012, ApJL, 750, L10
Testa, P., Saar, S. H., & Drake, J. J. 2015, RSPTA, 373, 20140259
Ugarte-Urra, I., Crump, N. A., Warren, H. P., & Wiegelmann, T. 2019, ApJ, 877, 129
Ugarte-Urra, I., & Warren, H. P. 2014, ApJ, 783, 12
Warren, H. P., Brooks, D. H., Doschek, G. A., & Feldman, U. 2016a, ApJ, 824, 56
Warren, H. P., Mariska, J. T., & Doschek, G. A. 2013, ApJ, 770, 116
Warren, H. P., Reep, J. W., Crump, N. A., & Simões, P. J. A. 2016b, ApJ, 829, 35
Warren, H. P., Winebarger, A. R., & Brooks, D. H. 2012, ApJ, 759, 141
Williams, T., Walsh, R. W., Winebarger, A. R., et al. 2020, ApJ, 892, 134
Wright, P. J., Hannah, I. G., Grefenstette, B. W., et al. 2017, ApJ, 844, 132